Stability of finite difference discretizations of multi-physics interface conditions

Björn Sjögreen[1,*], Jeffrey W. Banks[1]

[1]*Center for Applied Scientific Computing, Lawrence Livermore National Laboratory, Livermore, California, 94551*

Abstract. We consider multi-physics computations where the Navier-Stokes equations of compressible fluid flow on some parts of the computational domain are coupled to the equations of elasticity on other parts of the computational domain. The different subdomains are separated by well-defined interfaces. We consider time accurate computations resolving all time scales. For such computations, explicit time stepping is very efficient. We address the issue of discrete interface conditions between the two domains of different physics that do not lead to instability, or to a significant reduction of the stable time step size. Finding such interface conditions is non-trivial.
We discretize the problem with high order centered difference approximations with summation by parts boundary closure. We derive L^2 stable interface conditions for the linearized one dimensional discretized problem. Furthermore, we generalize the interface conditions to the full non-linear equations, and numerically demonstrate their stable and accurate performance on a simple model problem. The energy stable interface conditions derived here through symmetrization of the equations contain the interface conditions derived through normal mode analysis by Banks and Sjögreen in [7] as a special case.

AMS subject classifications: 65M12, 35L60, 35L65

1 Introduction

This work will consider numerical simulation of multi-physics systems where two, or more, physics models are solved on different parts of a computational domain. These different multi-physics domains are assumed to be separated by well-defined interfaces. Coupling conditions which join the various sub-domains are defined on these interfaces.

In the literature, there is a large body of work relating to numerical treatment of this type of fluid-structure interface. By far the most common approach is to apply material motions from the solid domain as boundary conditions to the fluid while using the

*Corresponding author. *Email addresses:* sjogreen2@llnl.gov, banks20@llnl.gov

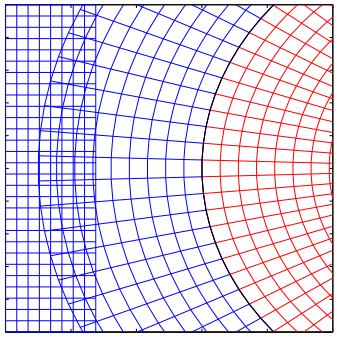

Figure 1: Graphic representation of one possible computational setup in two space dimensions. Blue represents the fluid and red represents the solid.

fluid stresses as boundary conditions on the solid. However, this approach can become problematic from a stability perspective for certain cases. As a result, implicit, sometimes referred to as monolithic, approaches have often been adopted. Such schemes are effective, but can introduce additional difficulties in terms of linear/nonlinear solvers and pre-conditioners.

Recent work in [6, 7] has shown that more symmetric approaches to interface condition imposition can result in favorable approximations, possibly with stability across all ranges of material parameters. The main purpose of the current work is to discuss the well-posedness of the continuous linearized fluid-structure problem and introduce a summation-by-parts discretization which mimics the energy behavior or the continuous operators. The operators which are thus derived have similar structure to those found in [7]. We will verify the accuracy of this new approach via manufactured solutions, and apply the schemes to a nontrivial problem of a Navier-Stokes fluid with an elastic-plastic solid.

The example studied here will be fluid/structure interaction in one space dimension, but the ideas are intended as more generally applicable. However, the techniques employed in this work have an impact on the discretization choices available for extension to, for example, two space dimensions. This is an important point and so we provide a brief discussion of these issues. The eventual numerical discretization of the governing equations and interface conditions investigated here requires a set of interface aligned grids. That is to say that the interface defining the boundary between two, or more, physics sub-domains must be represented in both computational sub-domains. This is shown graphically in Fig. 1. Here, the fluid equations are discretized on the blue grids and the solid is discretized on the red grid. The requirement that both computational sub-domains align with the material interface implies that other techniques are required to deal with external boundaries. In Fig. 1, we indicate that an overset grid approach [4] is used to treat the fluid domain, while a structured deforming grid is used for the solid.

Other options are of course possible and include embedded boundaries, overset grids, unstructured grids, or others. The key requirement as it relates to this work is that the fluid and solid are discretized on grids which align to the material interface.

The remainder of this work is structured as follows. Section 2 describes the equations in full generality. In Section 3, we perform an energy estimate of the one dimensional continuous problem, and prove that the standard interface conditions lead to a well-posed problem with decreasing energy. Section 4 performs the same analysis for finite difference discretizations that satisfy the summation by parts principle. We find energy stable discretizations and give explicit formulas for the discrete interface conditions. Section 5 shows numerical examples in one space dimension. The method of manufactured solution is first used to verify the implementation and to study the numerical convergence order obtained for finite difference schemes of different formal accuracies. Finally, we simulate an elastic rod pulled by gravity into a compressible fluid. Conclusions are presented in Section 6.

2 Equations

Let the updated Lagrangian equations of motion,

$$\begin{aligned}
\rho^{(s)}\mathbf{u}_t^{(s)} &= -\nabla p^{(s)} + \operatorname{div}\sigma + \rho^{(s)}\mathbf{f}^{(s)} \\
\sigma_t &= -W^{(s)}\sigma - \sigma(W^{(s)})^T + \lambda_e \operatorname{div}\mathbf{u}^{(s)} I + 2\mu_e D^{(s)} \\
\rho^{(s)}\epsilon_t &= -p^{(s)}\operatorname{div}\mathbf{u}^{(s)} + (\sigma : D^{(s)}) + \operatorname{div}(\kappa_e \nabla T^{(s)}) \\
\mathbf{x}_t &= \mathbf{u}^{(s)},
\end{aligned} \tag{2.1}$$

together with the algebraic relation $\rho^{(s)} J = \rho_0^{(s)} J_0 = m_0$, model the movement and deformation of an elastic-plastic body, see, e.g., [16]. The pressure, $p^{(s)}$, models plastic effects. The equations of structural mechanics for elastic materials, as described, e.g., in [2], are obtained from (2.1) by setting $p^{(s)} = 0$.

The density $\rho^{(s)}$, velocity $\mathbf{u}^{(s)}$, stress tensor σ, internal energy ϵ, and temperature $T^{(s)}$, are functions of $(\mathbf{X}, t)$. The Lagrangian coordinates $\mathbf{X} = (X_1,\ X_2,\ X_3)$ are the coordinates in a reference configuration at time zero. A volume distributed forcing is given by $\mathbf{f}^{(s)}$. The Eulerian coordinates

$$\mathbf{x} = \mathbf{x}(\mathbf{X}, t) \tag{2.2}$$

represent the position at time t of the material point that was located at $\mathbf{X}$ at time zero. The partial derivative of a variable with respect to t with $\mathbf{X}$ held fixed is denoted by subscript t. In the continuum mechanics literature these material time derivatives are often instead denoted by D/Dt.

The derivative of (2.2) is denoted by

$$(F)_{i,j} = \frac{\partial x_i}{\partial X_j}$$

and its Jacobian by $J = det(F)$. $m_0 = J_0\rho_0^{(s)}$ denotes $J(X,0)\rho^{(s)}(X,0)$. The gradient, ∇, and divergence operators act in the Eulerian coordinates, and can be evaluated in the Lagrangian frame by use of the coordinate mapping (2.2). I is the identity matrix, and the symmetric and skew-symmetric parts of the velocity gradient are defined as

$$D^{(s)} = \frac{1}{2}(\nabla \mathbf{u}^{(s)} + \nabla(\mathbf{u}^{(s)})^T) \quad \text{and} \qquad W^{(s)} = \frac{1}{2}(\nabla \mathbf{u}^{(s)} - \nabla(\mathbf{u}^{(s)})^T).$$

The Lamé parameters μ_e and λ_e are in general functions of the spatial coordinate, and depend on the material. A thermodynamic relation $\epsilon = \epsilon(T^{(s)})$ relates the temperature and internal energy. We will use a linear relation

$$\epsilon = \alpha T^{(s)}, \tag{2.3}$$

where α is a given constant. The pressure, when present, is given through an equation of state

$$p^{(s)} = p^{(s)}(\epsilon, \rho^{(s)}) \tag{2.4}$$

which is a function of the internal energy and density. The superscript s on the density, velocity, temperature, and pressure denotes that these are quantities defined in the elastic material.

The compressible Navier-Stokes equations,

$$\begin{aligned} \rho_t^{(f)} + \operatorname{div}\rho^{(f)}\mathbf{u}^{(f)} &= 0 \\ (\rho^{(f)}\mathbf{u}^{(f)})_t + \operatorname{div}(\rho^{(f)}\mathbf{u}^{(f)}(\mathbf{u}^{(f)})^T + p^{(f)}I) &= \operatorname{div}(\lambda \operatorname{div}\mathbf{u}^{(f)} I + 2\mu D^{(f)}) \\ e_t + \operatorname{div}(\mathbf{u}^{(f)}(e + p^{(f)})) &= \operatorname{div}(\lambda \mathbf{u}^{(f)} \operatorname{div}\mathbf{u}^{(f)} + 2\mu D^{(f)}\mathbf{u}^{(f)}) + \operatorname{div}(\kappa \nabla T^{(f)}) \end{aligned} \tag{2.5}$$

models the fluid. The superscript f on the density, velocity, temperature, and pressure denotes that the quantities are defined in the fluid part of the computational domain.

The pressure obeys the perfect gas law, $p^{(f)} = (\gamma - 1)(e - \rho^{(f)}|\mathbf{u}^{(f)}|^2/2)$, for a constant γ, where e is the total energy. The coefficients of viscosity are μ and λ, and κ is the heat conduction. λ is given by the zero bulk viscosity assumption $\lambda = -\frac{2}{3}\mu$. The equation of state $p^{(f)} = \frac{R}{M}\rho^{(f)}T^{(f)}$ is used to compute the temperature from the other variables. R is the universal gas constant, and M is the constant molar mass of the fluid. $D^{(f)}$ is the symmetric part of the velocity gradient of the fluid velocity. The dependent variables in (2.5) are functions of the Eulerian coordinates $(\mathbf{x}, t)$.

2.1 Interface conditions

The interface conditions at the fluid/solid boundary are the no-slip condition

$$\mathbf{u}^{(f)} = \mathbf{u}^{(s)}, \tag{2.6}$$

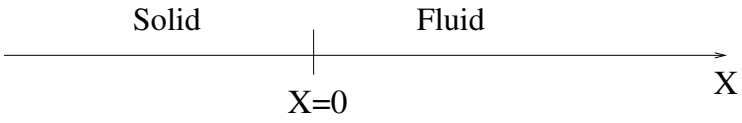

Figure 2: Domain for analysis of the one dimensional equations.

normal stress continuity

$$-p^{(f)}\mathbf{n}+\lambda \operatorname{div}\mathbf{u}^{(f)}\mathbf{n}+2\mu D^{(f)}\mathbf{n}=\sigma\mathbf{n}-p^{(s)}\mathbf{n}, \tag{2.7}$$

and continuity of the temperature and of the heat flux

$$T^{(f)}=T^{(s)} \tag{2.8}$$

$$\kappa\frac{\partial T^{(f)}}{\partial n}=\kappa_e\frac{\partial T^{(s)}}{\partial n}. \tag{2.9}$$

$\mathbf{n}$ is a unit vector normal to the interface, and $\partial/\partial n$ denotes the derivative in the direction $\mathbf{n}$ in the Eulerian coordinate.

3 Energy estimate in one space dimension

The interface conditions (2.6)-(2.9) are natural conditions from physics considerations, and should therefore lead to a well-posed problem. In this section we prove that this is indeed the case. Furthermore, the analysis gives insight into how to construct stable finite difference discretizations.

Consider the one-dimensional domain outlined in Fig. 2, where an interface at the Eulerian coordinate $x_I(t)$ separates a fluid to the right and an elastic-plastic solid to the left. In Lagrangian coordinates, the interface is given by $X=0$.

The equations (2.1), when restricted to one space dimension become

$$\begin{aligned} u_t^{(s)} &= \frac{1}{m_0}\left(\sigma-p^{(s)}\right)_X \\ \sigma_t &= \frac{1}{x_X}(2\mu_e+\lambda_e)u_X^{(s)} \\ m_0\epsilon_t &= \left(\sigma-p^{(s)}\right)u_X^{(s)}+\left(\frac{\kappa_e}{x_X}T_X^{(s)}\right)_X \\ x_t &= u^{(s)}, \end{aligned} \tag{3.1}$$

for the domain $-\infty<X<0$. Mass conservation in one dimension is $\rho^{(s)}x_X=m_0$, because $J=x_X$.

The fluid equations (2.5) are transformed to the coordinate X by the moving coordinate mapping $x = X + x_I(t)$, i.e., to a rigid frame that moves with the interface, and become

$$\begin{aligned} \rho_t^{(f)} + \left(\rho^{(f)} u^{(f)} - s_I(t)\rho^{(f)}\right)_X &= 0 \\ \left(\rho^{(f)} u^{(f)}\right)_t + \left(\rho^{(f)}(u^{(f)})^2 + p^{(f)} - s_I(t)\rho^{(f)} u^{(f)}\right)_X &= \frac{4}{3}\mu u_{XX}^{(f)} \\ e_t + \left(u^{(f)}(e+p^{(f)}) - s_I(t)e\right)_X &= \frac{4}{3}\mu\left(u^{(f)} u_X^{(f)}\right)_X + \left(\kappa T_X^{(f)}\right)_X \end{aligned} \tag{3.2}$$

on the domain $0 < X < \infty$. In (3.2), $s_I(t)$ denotes the interface velocity $dx_I(t)/dt$.

3.1 Linearized problem

The Navier-Stokes equations (3.2) can be reformulated in the variables $(\rho^{(f)},\, u^{(f)},\, T^{(f)})$, and become

$$\begin{aligned} &\rho_t^{(f)} + \left(u^{(f)} - s(t)\right)\rho_X^{(f)} + \rho^{(f)} u_X^{(f)} = 0 \\ &u_t^{(f)} + \left(u^{(f)} - s(t)\right)u_X^{(f)} + \frac{1}{\rho^{(f)}} p_X^{(f)} = \frac{1}{\rho^{(f)}}\frac{4}{3}\mu u_{XX}^{(f)} \\ &T_t^{(f)} + \left(u^{(f)} - s(t)\right)T_X^{(f)} + (\gamma-1)T^{(f)} u_X^{(f)} = \frac{M}{R}\frac{\gamma-1}{\rho^{(f)}}\left(\frac{4}{3}\mu\left(u_X^{(f)}\right)^2 + \left(\kappa T_X^{(f)}\right)_X\right). \end{aligned} \tag{3.3}$$

Linearization is accomplished by considering

$$(\rho^{(f)},\, u^{(f)},\, T^{(f)}) = (\hat{\rho}^{(f)},\, \hat{u}^{(f)},\, \hat{T}^{(f)}) + (\rho^{(f)'},\, u^{(f)'},\, T^{(f)'}) \tag{3.4}$$

where $(\hat{\rho}^{(f)},\, \hat{u}^{(f)},\, \hat{T}^{(f)})$ is a constant state, and $(\rho^{(f)'},\, u^{(f)'},\, T^{(f)'})$ is a small perturbation. The interface velocity is also linearized about the constant $\hat{u}^{(f)}$ as $s = \hat{u}^{(f)} + s'$. The equation of state is linearized according to

$$p^{(f)} = \frac{R}{M}(\hat{T}^{(f)} + T^{(f)'})(\hat{\rho}^{(f)} + \rho^{(f)'}) = \frac{R}{M}\hat{T}^{(f)}\hat{\rho}^{(f)} + \frac{R}{M}\hat{\rho}^{(f)} T^{(f)'} + \frac{R}{M}\hat{T}^{(f)}\rho^{(f)'} + \ldots,$$

where terms that are quadratic in the small perturbation have been neglected. We identify constant and leading order fluid pressure

$$\hat{p}^{(f)} = \frac{R}{M}\hat{T}^{(f)}\hat{\rho}^{(f)} \quad \text{and} \quad p^{(f)'} = \frac{R}{M}\hat{\rho}^{(f)} T^{(f)'} + \frac{R}{M}\hat{T}^{(f)}\rho^{(f)'}. \tag{3.5}$$

We insert (3.4) and the linearized interface velocity into (3.3) and neglect perturbation terms occurring with powers two or higher. The final result is the linearized system

$$\begin{aligned}
&\rho_t^{(f)'} + \hat{\rho}^{(f)} u_X^{(f)'} = 0 \\
&u_t^{(f)'} + \frac{R}{M} T_X^{(f)'} + \frac{R\hat{T}^{(f)}}{M\hat{\rho}^{(f)}} \rho_X^{(f)'} = \frac{1}{\hat{\rho}^{(f)}} \frac{4}{3} \mu u_{XX}^{(f)'} \\
&T_t^{(f)'} + (\gamma - 1)\hat{T}^{(f)} u_X^{(f)'} = \frac{M}{R} \frac{\gamma - 1}{\hat{\rho}^{(f)}} \left((\kappa T_X^{(f)'})_X \right),
\end{aligned} \tag{3.6}$$

for $0 < X$.

Similarly, for (3.1) we first rewrite the energy equation as an equation for the temperature by substituting $\epsilon = \alpha T^{(s)}$ in the last equation and perform the linearization

$$(u^{(s)}, \sigma, T^{(s)}) = (\hat{u}^{(s)}, \hat{\sigma}, \hat{T}^{(s)}) + (u^{(s)'}, \sigma', T^{(s)'}) \tag{3.7}$$

$$x = X + \hat{u}^{(s)} t + x', \tag{3.8}$$

where $(\hat{u}^{(s)}, \hat{\sigma}, \hat{T}^{(s)})$ is a constant state. Hence, the coordinate mapping is linearized around a uniform reference configuration. Taking the spatial derivative of (3.8) gives $x_X = 1 + x'_X$, and we also obtain the linearization of $1/x_X$ as $1 - x'_X$. The density, which satsifies $\rho^{(s)} x_X = m_0$, is linearized as

$$\rho^{(s)} = m_0 / x_X = m_0 (1 - x'_X) = m_0 - m_0 x'_X,$$

and hence we define $\hat{\rho}^{(s)} = m_0$ and $\rho^{(s)'} = -\hat{\rho}^{(s)} x'_X$. The pressure, $p^{(s)} = p^{(s)}(\epsilon, \rho^{(s)})$ is linearized as

$$p^{(s)} = \hat{p}^{(s)} + \hat{p}_\rho^{(s)} \rho^{(s)'} + \hat{p}_\epsilon^{(s)} \epsilon' = \hat{p}^{(s)} - \hat{p}_\rho^{(s)} \hat{\rho}^{(s)} x'_X + \alpha \hat{p}_\epsilon^{(s)} T^{(s)'},$$

where $\hat{p}_\epsilon^{(s)}$ $\hat{p}_\rho^{(s)}$ are the partial derivatives of the equation of state as a function $p^{(s)} = p^{(s)}(\epsilon, \rho^{(s)})$ evaluated at the linearization state. The linearization of the system (3.1) becomes

$$\begin{pmatrix} u^{(s)'} \\ \sigma' \\ T^{(s)'} \\ x'_X \end{pmatrix}_t = \begin{pmatrix} 0 & 1/m_0 & -\alpha \hat{p}_\epsilon^{(s)} / m_0 & \hat{p}_\rho^{(s)} \\ (2\mu_e + \lambda_e) & 0 & 0 & 0 \\ \frac{\hat{\sigma} - \hat{p}^{(s)}}{\alpha m_0} & 0 & 0 & 0 \\ 1 & 0 & 0 & 0 \end{pmatrix} \begin{pmatrix} u^{(s)'} \\ \sigma' \\ T^{(s)'} \\ x'_X \end{pmatrix}_X + \begin{pmatrix} 0 \\ 0 \\ \frac{\kappa_e}{\alpha m_0} T_{XX}^{(s)'} \\ 0 \end{pmatrix} \tag{3.9}$$

for $X < 0$. We have taken a spatial derivative of the last equation. In the case when $\hat{p}_\rho^{(s)} = 0$, the equation for the coordinate mapping is not coupled to the equations for $(u^{(s)'}, \sigma', T^{(s)'})$. In the remainder of this section we will simplify the notation by dropping the primes on the perturbation variables and consider the systems (3.6) and (3.9) on $X >$

0 and $X<0$ respectively. Note that the linearization states should satisfy the interface conditions. In particular, $\hat{u}^{(s)}=\hat{u}^{(f)}$ and $\hat{T}^{(s)}=\hat{T}^{(f)}$.

We introduce the vector of unknows in the fluid and the solid respectively as $\mathbf{q}^{(f)}=(\rho^{(f)}, u^{(f)}, T^{(f)})$ and $\mathbf{q}^{(s)}=(u^{(s)}, \sigma, T^{(s)}, x_X)$, and rewrite (3.6) and (3.9) in matrix form as

$$\mathbf{q}_t^{(s)}+A_s\mathbf{q}_X^{(s)}=B_s\mathbf{q}_{XX}^{(s)} \quad X<0 \tag{3.10}$$

$$\mathbf{q}_t^{(f)}+A_f\mathbf{q}_X^{(f)}=B_f\mathbf{q}_{XX}^{(f)} \quad X>0, \tag{3.11}$$

where the definition of the matrices A_s, B_s, A_f, and B_f are immediate from (3.6) and (3.9). B_s and B_f are diagonal matrices. The eigenvalues of A_f are $\hat{u}^{(f)}-\hat{c}$, $\hat{u}^{(f)}$, $\hat{u}^{(f)}+\hat{c}$ where $\hat{c}=\sqrt{\gamma\hat{p}^{(f)}/\hat{\rho}^{(f)}}$, which shows that the fluid equations are hyperbolic in the inviscid limit for positive pressure and density. A_s has eigenvalues 0,0, $-c^{(s)}$, and $c^{(s)}$, where

$$(c^{(s)})^2=\frac{2\mu_e+\lambda_e}{m_0}+\frac{\hat{p}^{(s)}-\hat{\sigma}}{m_0^2}\hat{p}_\epsilon^{(s)}+\hat{p}_\rho^{(s)}.$$

Because $\hat{p}^{(f)}>0$, linearization around a reference state with $\hat{p}^{(s)}-\hat{\sigma}=\hat{p}^{(f)}$ guarantees that $\hat{p}^{(s)}-\hat{\sigma}>0$. Hence, $(c^{(s)})^2>0$ and A_s has real eigenvalues under the additional assumptions $\hat{p}_\epsilon^{(s)}>0$ and $\hat{p}_\rho^{(s)}>0$. This is true for example with the ideal gas law $p^{(s)}=(\gamma-1)\rho^{(s)}\epsilon$.

At $X=0$ the interface conditions (2.6), (2.8), and (2.9) are unchanged for the linearized problem. Linearization of (2.7) around the reference state with $\hat{p}^{(f)}=\hat{p}^{(s)}-\hat{\sigma}$ gives

$$-\frac{\hat{T}^{(f)}R}{M}\rho^{(f)}-\frac{\hat{\rho}^{(f)}R}{M}T^{(f)}+\frac{4\mu}{3}u_x^{(f)}=\sigma-\hat{p}_\epsilon^{(s)}\alpha T^{(s)}-\hat{p}_\rho^{(s)}\rho^{(s)}. \tag{3.12}$$

In order to prove an energy estimate, we first transform the systems (3.10) and (3.11) to symmetric form. This is done by the diagonal matrix

$$Y_s=diag\left(1/\sqrt{m_0},\sqrt{2\mu_e+\lambda_e},\sqrt{\hat{p}^{(s)}-\hat{\sigma}}/(\alpha\sqrt{m_0\hat{p}_\epsilon^{(s)}}),1/\sqrt{m_0\hat{p}_\rho^{(s)}}\right) \tag{3.13}$$

for (3.10) and by

$$Y_f=diag\left(\sqrt{\hat{\rho}^{(f)}M/(R\hat{T}^{(f)})},1/\sqrt{\hat{\rho}^{(f)}},\sqrt{(\gamma-1)\hat{T}^{(f)}M/(\hat{\rho}^{(f)}R)}\right) \tag{3.14}$$

for (3.11). Denote $\mathbf{w}^{(s)}=Y_s^{-1}\mathbf{q}^{(s)}$ and $\mathbf{w}^{(f)}=Y_f^{-1}\mathbf{q}^{(f)}$. The symmetrized equations,

$$\mathbf{w}_t^{(s)}+S_s\mathbf{w}_X^{(s)}=B_s\mathbf{w}_{XX}^{(s)} \quad X<0 \tag{3.15}$$

$$\mathbf{w}_t^{(f)}+S_f\mathbf{w}_X^{(f)}=B_f\mathbf{w}_{XX}^{(f)} \quad X>0, \tag{3.16}$$

are obtained by left multiplication of (3.10) and (3.11) by Y_s^{-1} and Y_f^{-1} respectively. The symmetric matrices are

$$S_s = \begin{pmatrix} 0 & -\sqrt{\frac{2\mu_e+\lambda_e}{m_0}} & \frac{\sqrt{\hat{p}_\epsilon^{(s)}\hat{p}^{(s)}}}{m_0} & -\sqrt{\hat{p}_\rho^{(s)}} \\ . & 0 & 0 & 0 \\ . & . & 0 & 0 \\ . & . & . & 0 \end{pmatrix} \qquad S_f = \begin{pmatrix} 0 & \sqrt{\frac{R\hat{T}^{(f)}}{M}} & 0 \\ . & 0 & \sqrt{\frac{R(\gamma-1)\hat{T}^{(f)}}{M}} \\ . & . & 0 \end{pmatrix}$$

for the solid and fluid respectively. B_s and B_f are unchanged by the symmetrizing transformation, because they are diagonal.

Define the scalar product for any two functions on $X<0$ by

$$(p,q)_- = \int_{-\infty}^{0} p(X,t)q(X,t)dX,$$

and similarly on $X>0$,

$$(p,q)_+ = \int_{0}^{\infty} p(X,t)q(X,t)dX.$$

The corresponding norms are denoted by $||q||_-^2 = (q,q)_-$ and $||q||_+^2 = (q,q)_+$. The following theorem states well-posedness of the linearized fluid/structure problem.

Theorem 3.1. *Consider the equations (3.16) for $X>0$ and (3.15) for $X<0$, coupled by (2.6), (3.12), (2.8), and (2.9) at $X=0$. Assume that the solutions vanish when $X\to\pm\infty$. Furthermore, assume that $p^{(s)}(\epsilon,\rho^{(s)})$ has positive partial derivatives, $p_\epsilon^{(s)}>0$ and $p_\rho^{(s)}>0$. Then the estimate*

$$||\mathbf{w}^{(s)}(t)||_-^2 + ||\mathbf{w}^{(f)}(t)||_+^2 \le ||\mathbf{w}^{(s)}(0)||_-^2 + ||\mathbf{w}^{(f)}(0)||_+^2 \tag{3.17}$$

holds for all $t>0$.

Proof: The standard estimate

$$\begin{aligned} \frac{1}{2}\frac{d}{dt}||\mathbf{w}||^2 = (\mathbf{w},\mathbf{w}_t) &= -(\mathbf{w},S\mathbf{w}_x) + (\mathbf{w},B\mathbf{w}_{xx}) \\ &= -\frac{1}{2}\mathbf{w}^T S\mathbf{w}|_b - (\mathbf{w}_x,B\mathbf{w}_x) + \mathbf{w}^T B\mathbf{w}_x|_b, \end{aligned} \tag{3.18}$$

for the PDE $\mathbf{w}_t + S\mathbf{w}_x = B\mathbf{w}_{xx}$ with symmetric S holds, because integration by parts and the symmetry of S give

$$(\mathbf{w},S\mathbf{w}_x) = -(\mathbf{w}_x,S\mathbf{w}) + \mathbf{w}^T S\mathbf{w}|_b = -(S\mathbf{w}_x,\mathbf{w}) + \mathbf{w}^T S\mathbf{w}|_b$$

and $(\mathbf{w},S\mathbf{w}_x)=(1/2)\mathbf{w}^T S\mathbf{w}|_b$ follows. The notation $|_b$ denotes restriction to the boundary. It follows that

$$\frac{1}{2}\frac{d}{dt}\left(||\mathbf{w}^{(s)}(t)||_-^2+||\mathbf{w}^{(f)}(t)||_+^2\right)= \frac{1}{2}\left(-(\mathbf{w}^{(s)})^T S_s\mathbf{w}^{(s)}|_0+(\mathbf{w}^{(f)})^T S_f\mathbf{w}^{(f)}|_0\right)+(\mathbf{w}^{(s)})^T B_s\mathbf{w}_x^{(s)}|_0 -(\mathbf{w}^{(f)})^T B_f\mathbf{w}_x^{(f)}|_0-(\mathbf{w}_x^{(s)},B_s\mathbf{w}_x^{(s)})_- -(\mathbf{w}_x^{(f)},B_f\mathbf{w}_x^{(f)})_+, \quad (3.19)$$

where $|_0$ is restriction to $X=0$. The interface condition is obtained by requiring

$$\frac{1}{2}\left(-(\mathbf{w}^{(s)})^T S_s\mathbf{w}^{(s)}|_0+(\mathbf{w}^{(f)})^T S_f\mathbf{w}^{(f)}|_0\right)+(\mathbf{w}^{(s)})^T B_s\mathbf{w}_x^{(s)}|_0-(\mathbf{w}^{(f)})^T B_f\mathbf{w}_x^{(f)}|_0=0,$$

which written out in terms of the original variables is equivalent to

$$\frac{1}{2}u^{(s)}\left(\sigma-\hat{p}_\rho^{(s)}\rho^{(s)}-\alpha\hat{p}_\epsilon^{(s)}T^{(s)}\right)+\frac{1}{2}u^{(f)}\left(\frac{R}{M}\hat{T}^{(f)}\rho^{(f)}+\frac{R}{M}\hat{\rho}^{(f)}T^{(f)}-\frac{4}{3}\mu u_X^{(f)}\right)+ \frac{1}{\hat{T}}\kappa_e T^{(s)}T_X^{(s)}-\frac{1}{\hat{T}}\kappa T^{(f)}T_X^{(f)}=0, \quad (3.20)$$

where all variables are evaluated at $X=0$. It is straightforward to verify that interface conditions (2.6) , (3.12), (2.8), and (2.9) indeed make the left hand side of (3.20) equal to zero. The remaining terms of (3.19) give,

$$\frac{1}{2}\frac{d}{dt}\left(||\mathbf{w}^{(s)}(t)||_-^2+||\mathbf{w}^{(f)}(t)||_+^2\right)=-(\mathbf{w}_x^{(s)},B_s\mathbf{w}_x^{(s)})_- -(\mathbf{w}_x^{(f)},B_f\mathbf{w}_x^{(f)})_+\leq 0,$$

because B_f and B_s are positive semi-definite. The energy estimate (3.17) follows. □

4 Discretization in one space dimension

Introduce a uniform grid with grid spacing h on the domain in Fig. 2, in the Lagrangian coordinate, $X_j=jh$. Let the fluid/structure interface be located at the grid point $j=0$. The dependent variables of the fluid equations at the grid point X_j, $(\rho_j^{(f)},\ \rho_j^{(f)}u_j^{(f)},\ e_j)$, are defined for $j\geq 0$ and the dependent variables of the elasticity equations, $(u_j^{(s)},\ \sigma_j,\ \epsilon_j,\ x_j)$ are defined for $j\leq 0$. Hence, both solid and fluid variables are defined at the interface grid point $X_0=0$.

4.1 Discretization by summation-by-parts finite differences

Consider the domain $j\leq 0$. A summation-by-parts finite difference operator is a difference operator approximating d/dx, D_L, that satisfies

$$(u,D_L v)_{h-}=-(D_L u,v)_{h-}+u_0v_0 \quad (4.1)$$

for grid functions u_j and v_j defined on $j \le 0$. The discrete weighted scalar product is defined on $j \le 0$ by,

$$(u,v)_{h-} = h \sum_{j=-\infty}^{0} a_j^{(-)} u_j v_j.$$

Here D_L is a standard centered difference operator away from the boundary. Near the boundary $j = 0$, D_L is biased toward the left and only uses function values with $j \le 0$. The weights in the norm $a_j^{(-)} > 0$ are equal to one away from the boundary, and are modified to satisfy (4.1) near the boundary. For details on how to derive operators and scalar products, see [11,15], where example operators of orders up to 4 at the boundaries and up to 8 away from the boundaries are given. The scalar product for $j \ge 0$ is defined similarly as

$$(u,v)_{h+} = h \sum_{j=0}^{\infty} a_j^{(+)} u_j v_j,$$

and a finite difference operator on $j \ge 0$, biased to the right at $j = 0$, D_R, can be made to satisfy

$$(u, D_R v)_{h+} = -(D_R u, v)_{h+} - u_0 v_0$$

for grid functions, u_j and v_j defined on $j \ge 0$. The corresponding discrete norms are denoted by $||u||_{h-}^2 = (u,u)_{h-}$ and $||u||_{h+}^2 = (u,u)_{h+}$.

The semi-discrete approximation of (3.11) and (3.10) is obtained by replacing all spatial derivatives by SBP difference operators. In the SBP framework, boundary conditions can be imposed by projection [11], by a penalty term (so called SAT boundary condition) [3], or by use of a ghost point [10]. Here, we use projections to impose the interface conditions at $j = 0$. The projection method introduces a projection operator, P, that projects a general grid function onto the set of grid functions that satisfy the interface conditions. This operator is applied after each time step. In a semi-discrete approximation, this amounts to solving the equations

$$\frac{d}{dt}\mathbf{q}_j^{(s)} + P_s A_s D_L \mathbf{q}_j^{(s)} = P_s B_s D_L^2 \mathbf{q}_j^{(s)} \quad j \le 0 \tag{4.2}$$

$$\frac{d}{dt}\mathbf{q}_j^{(f)} + P_f A_f D_R \mathbf{q}_j^{(f)} = P_f B_f D_R^2 \mathbf{q}_j^{(f)} \quad j \ge 0, \tag{4.3}$$

where P_s and P_f are the projections on the solid and fluid variables respectively.

Here we have approximated the second derivatives by two applications of the first difference operator. The advantage of this approach is that it is easy to generalize to the case of variable coefficients, e.g., when the viscosity depends on the temperature. The repeated first difference approximation does not damp the highest modes, but the discretization is still stable. Indeed, our results below show stability, and even boundedness of the solution for all times, in the L^2 norm for the linearized discretized problem (4.2), (4.3) coupled by an interface condition. The proof of stability only holds for the

linear problem, the theory is less complete for non-linear PDEs. However, numerical experiments with the non-linear Euler and Navier-Stokes equations of gas dynamics have shown that repeated application of D_L for second derivatives in the Navier-Stokes viscosity can supress non-linear instabilities, see, e.g., [13]. If damping of the highest modes is desired, the narrow stencil summation by parts operator recently developed in [12] can be used in (4.2) and (4.3) instead.

The discrete form of the interface conditions is

$$u_0^{(s)} = u_0^{(f)} \tag{4.4}$$

$$\sigma_0 - \hat{p}_e^{(s)} \alpha T_0^{(s)} - \hat{p}_\rho^{(s)} \rho_0^{(s)} = -\frac{\hat{T}^{(f)} R}{M} \rho_0^{(f)} - \frac{\hat{\rho}^{(f)} R}{M} T_0^{(f)} + \frac{4\mu}{3} D_R u_0^{(f)} \tag{4.5}$$

$$T_0^{(s)} = T_0^{(f)} \tag{4.6}$$

$$\kappa_e D_L T_0^{(s)} = \kappa D_R T_0^{(f)}. \tag{4.7}$$

The following theorem states that if the projections are applied in the symmetric variables, an energy estimate follows.

Theorem 4.1. *Define $P_s = Y_s Q_s Y_s^{-1}$ and $P_f = Y_f Q_f Y_f^{-1}$, where Q_s and Q_f are projections to the interface condition acting on the symmetric variables, i.e., grid functions $(Q_s \mathbf{w}^{(s)}, Q_f \mathbf{w}^{(f)})$ that satisfy the discrete interface conditions (4.4)–(4.7), and minimize $||\mathbf{w}^{(s)} - Q_s \mathbf{w}^{(s)}||_{h-}^2 + ||\mathbf{w}^{(f)} - Q_f \mathbf{w}^{(f)}||_{h+}^2$. Then the energy estimate for the symmetric variables in the discrete norm,*

$$\frac{d}{dt}\left(||\mathbf{w}^{(s)}(t)||_{h-}^2 + ||\mathbf{w}^{(f)}(t)||_{h+}^2 \right) \leq 0$$

holds.

Proof: The first step is to transform (4.2) and (4.3) to symmetric form by left multiplication of (3.13) and (3.14). Symmetrization of the elasticity equations ($j \leq 0$) gives

$$\frac{d}{dt}\mathbf{w}_j^{(s)} + Y_s^{-1} P_s Y_s S_s D_L \mathbf{w}_j^{(s)} = Y_s^{-1} P_s Y_s B_s D_L^2 \mathbf{w}_j^{(s)},$$

and hence

$$\frac{d}{dt}\mathbf{w}_j^{(s)} + Q_s S_s D_L \mathbf{w}_j^{(s)} = Q_s B_s D_L^2 \mathbf{w}_j^{(s)}. \tag{4.8}$$

Multiplication of (4.8) by Q_s and the projection property $Q_s^2 = Q_s$ show that

$$\frac{d}{dt}\left(\mathbf{w}_j^{(s)} - Q_s \mathbf{w}_j^{(s)} \right) = 0 \Rightarrow \mathbf{w}_j^{(s)}(t) = Q_s \mathbf{w}_j^{(s)}(t). \tag{4.9}$$

if the initial data satisfies the interface conditions. The estimate for $j \leq 0$ becomes,

$$\begin{aligned}\frac{1}{2}\frac{d}{dt}||\mathbf{w}^{(s)}(t)||_{h-}^2 &= \left(\mathbf{w}^{(s)}, \mathbf{w}_t^{(s)}\right)_{h-} = -\left(Q_s S_s D_L \mathbf{w}^{(s)}, \mathbf{w}^{(s)}\right)_{h-} \\ &+ \left(Q_s B_s D_L^2 \mathbf{w}^{(s)}, \mathbf{w}^{(s)}\right)_{h-} = -\left(S_s D_L \mathbf{w}^{(s)}, \mathbf{w}^{(s)}\right)_{h-} + \left(B_s D_L^2 \mathbf{w}^{(s)}, \mathbf{w}^{(s)}\right)_{h-} \\ &- \left((Q_s - I) S_s D_L \mathbf{w}^{(s)}, \mathbf{w}^{(s)}\right)_{h-} + \left((Q_s - I) B_s D_L^2 \mathbf{w}^{(s)}, \mathbf{w}^{(s)}\right)_{h-} \end{aligned} \tag{4.10}$$

where the last two terms are zero because of (4.9), and the orthogonality of the projection. The SBP property (4.1) gives

$$\begin{aligned}\frac{1}{2}\frac{d}{dt}||\mathbf{w}^{(s)}(t)||_{h-}^2 &= -\left(S_s D_L \mathbf{w}^{(s)}, \mathbf{w}^{(s)}\right)_{h-} + \left(B_s D_L^2 \mathbf{w}^{(s)}, \mathbf{w}^{(s)}\right)_{h-} \\ &= -\frac{1}{2}(\mathbf{w}_0^{(s)})^T S_s \mathbf{w}_0^{(s)} + (\mathbf{w}^{(s)})_0^T B_s D_L \mathbf{w}_0^{(s)} - \left(D_L \mathbf{w}^{(s)}, B_s D_L \mathbf{w}^{(s)}\right)_{h-} \end{aligned} \tag{4.11}$$

in the same way as partial integration gives the estimate for the continuous problem. The estimate for the fluid equations on $j \geq 0$ is analogouos and is not give here. The resulting discrete interface condition,

$$-\frac{1}{2}(\mathbf{w}_0^{(s)})^T S_s \mathbf{w}_0^{(s)} + \frac{1}{2}(\mathbf{w}_0^{(f)})^T S_f \mathbf{w}_0^{(f)} + (\mathbf{w}_0^{(s)})^T B_s D_L \mathbf{w}_0^{(s)} - (\mathbf{w}_0^{(f)})^T B_f D_R \mathbf{w}_0^{(f)} = 0, \tag{4.12}$$

eliminates all interface contributions to the time derivative of the norm. Written out in original variables, (4.12) becomes identical to (3.20) evaluated at j=0 and with derivatives in X replaced by D_L or D_R for solid or fluid variables respectively. It is straightforward to verify that (4.4)–(4.7) satisfy (4.12). Therefore, the interface terms do not give any contribution to the time derivative of the norm, and the estimate follows. □

In each time step (or Runge-Kutta stage) in the fully discretized computation, the solution is first updated at all grid points, including the interface point $j = 0$, and then this updated solution is projected to the interface conditions. The projection for the temperatures means solving the two equations (4.6), (4.7) directly for the two temperatures $T_0^{(s)}$ and $T_0^{(f)}$. There is always a unique solution, because the coefficients of the $j = 0$ element in the completely backward operator D_L and the completely forward operator D_R have opposite signs. Let us denote the variables after the application of the SBP discretization but before imposing the interface condition by $\tilde{\mathbf{w}}$. Denote the difference operator approximating $du/dx(x_0)$ by

$$D_R u_0 = \frac{1}{h}\sum_{k=0}^{r} \beta_k u_k$$

where $r+1$ is the stencil width.

Theorem 4.2. *Assume that the interface temperature has been determined by (4.6) and (4.7). Furthermore, assume that $p^{(s)}=0$, i.e., that the solid is purely elastic. Then the interface conditions (4.4) and (4.5) imposed as a projection lead to*

$$u_0^{(s)} = \tilde{u}_0^{(s)} - l_1/(a_0^{(+)} m_0) \quad \sigma_0 = \tilde{\sigma}_0 - (2\mu_e + \lambda_e) l_2 / a_0^{(+)} \tag{4.13}$$

for the variables in the solid. Similarly, the projection gives the update

$$u_0^{(f)} = \tilde{u}_0^{(f)} + l_1/(a_0^{(+)}\hat{\rho}^{(f)}) + l_2 \frac{4\mu}{3\hat{\rho}^{(f)}} \frac{\beta_0}{a_0^{(+)} h} \quad u_j^{(f)} = \tilde{u}_j^{(f)} + l_2 \frac{4\mu}{3\hat{\rho}^{(f)}} \frac{\beta_0}{a_j^{(+)} h}, \quad j = 1, \ldots, r \tag{4.14}$$

for the fluid velocity, and

$$\rho_0^{(f)} = \tilde{\rho}_0^{(f)} - \hat{\rho}^{(f)} l_2 / a_0^{(+)} \tag{4.15}$$

for the fluid density. The quantities l_1 and l_2 are two Lagrangian multipliers obtained as the solution of the linear system of equations

$$\left(\frac{1}{m_0} + \frac{1}{\hat{\rho}^{(f)}} \right) \frac{1}{a_0^{(+)}} l_1 + \frac{4\mu}{3 a_0^{(+)} \hat{\rho}^{(f)}} \frac{\beta_0}{h} l_2 = \tilde{u}_0^{(s)} - \tilde{u}_0^{(f)} \tag{4.16}$$

$$\frac{4\mu}{3\hat{\rho}^{(f)}} \frac{\beta_0}{a_0^{(+)} h} l_1 + \left(2\mu_e + \lambda_e + \frac{R\hat{T}^{(f)}\hat{\rho}^{(f)}}{M} + \frac{16\mu^2}{9\hat{\rho}^{(f)} h^2} \sum_{k=0}^{r} \frac{a_0^{(+)}}{a_k^{(+)}} \beta_k^2 \right) \frac{l_2}{a_0^{(+)}} =$$

$$\tilde{\sigma}_0 + \frac{R\hat{T}^{(f)}}{M} \tilde{\rho}_0^{(f)} + \frac{R\hat{\rho}^{(f)}}{M} T_0 - \frac{4\mu}{3} D_R \tilde{u}_0^{(f)}. \tag{4.17}$$

Proof: The projections are defined as functions $\mathbf{w}^{(s)}$ and $\mathbf{w}^{(f)}$ that minimize

$$||\tilde{\mathbf{w}}^{(s)} - \mathbf{w}^{(s)}||_{h-}^2 + ||\tilde{\mathbf{w}}^{(f)} - \mathbf{w}^{(f)}||_{h+}^2$$

and satisfy the interface conditions (4.4) and (4.5). The interface conditions written out as constraints, for the case $p^{(s)} = 0$, are

$$u_0^{(s)} - u_0^{(f)} = 0 \tag{4.18}$$

$$\sigma_0 + \frac{\hat{T}^{(f)} R}{M} \rho_0^{(f)} + \frac{\hat{\rho}^{(f)} R}{M} T_0^{(f)} - \frac{4\mu}{3} D_R u_0^{(f)} = 0 \tag{4.19}$$

The solution of the constrained minimization problem is a stationary point of the Lagrangian function

$$\frac{1}{2}||\tilde{\mathbf{w}}^{(s)} - \mathbf{w}^{(s)}||_{h-}^2 + \frac{1}{2}||\tilde{\mathbf{w}}^{(f)} - \mathbf{w}^{(f)}||_{h+}^2 +$$

$$l_1 \left(u_0^{(s)} - u_0^{(f)} \right) +$$

$$l_2 \left(\sigma_0 + \frac{R\hat{T}^{(f)}}{M} \rho_0^{(f)} + \frac{\hat{\rho}^{(f)} R}{M} T_0 - \frac{4\mu}{3} D_R u_0^{(f)} \right). \tag{4.20}$$

This function is formed as the sum of the quantity to be minimized, and the constraints (4.18) and (4.19), multiplied by the Lagrangian multipliers l_1 and l_2 respectively. The stationary point is found as the zero of the gradient of (4.20), where the independent variables are $u_j^{(s)}$,σ_j for $j \leq 0$, $u_j^{(f)}$,$\rho_j^{(f)}$ for $j \geq 0$, l_1, and l_2. The temperature is assumed to be already determined by (4.6) and (4.7) and is therefore not considered to be an independent variable. Writing out the norm expressions, using symmetric variables and leaving out the temperature, lead to the explicit expression

$$\begin{aligned}\mathcal{L} = &\frac{1}{2}\sum_{j=-\infty}^{0} a_j^{(-)}\left(\sqrt{m_0}(\tilde{u}_j^{(s)} - u_j^{(s)})\right)^2 + \frac{1}{2}\sum_{j=0}^{\infty} a_j^{(+)}\left(\sqrt{\hat{\rho}^{(f)}}(\tilde{u}_j^{(f)} - u_j^{(f)})\right)^2 \\ &+ \frac{1}{2}\sum_{j=-\infty}^{0} a_j^{(-)}\left(\frac{1}{2\mu_e + \lambda_e}(\tilde{\sigma}_j^{(s)} - \sigma_j^{(s)})\right)^2 + \frac{1}{2}\sum_{j=0}^{\infty} a_j^{(+)}\left(\sqrt{\frac{R\hat{T}^{(f)}}{M\hat{\rho}^{(f)}}}(\tilde{\rho}_j^{(f)} - \rho_j^{(f)})\right)^2 \\ &+ l_1\left(u_0^{(s)} - u_0^{(f)}\right) + l_2\left(\sigma_0 + \frac{R\hat{T}^{(f)}}{M}\rho_0^{(f)} + \frac{\hat{\rho}^{(f)}R}{M}T_0 - \frac{4\mu}{3}D_R u_0^{(f)}\right) \end{aligned} \tag{4.21}$$

for (4.20). The only variables that need to be modified are the ones that appear in the interface conditions (4.18) or (4.19). For example, differentiation with respect to $u_{-2}^{(s)}$ gives

$$\frac{\partial \mathcal{L}}{\partial u_{-2}^{(s)}} = -a_{-2}^{(-)} m_0 \left(\tilde{u}_{-2}^{(s)} - u_{-2}^{(s)}\right)$$

which is zero for $u_{-2}^{(s)} = \tilde{u}_{-2}^{(s)}$. It is straightforward to see that the same is true for any variable $u_j^{(s)}$, σ_j, $u_j^{(f)}$, or $\rho_j^{(f)}$ appearing in neither (4.18) nor (4.19). The zero gradient condition

$$\frac{\partial \mathcal{L}}{\partial u_0^{(s)}} = -m_0 a_0^{(-)}\left(\tilde{u}_0^{(s)} - u_0^{(s)}\right) + l_1 = 0 \tag{4.22}$$

$$\frac{\partial \mathcal{L}}{\partial u_0^{(f)}} = -\hat{\rho}^{(f)} a_0^{(+)}\left(\tilde{u}_0^{(f)} - u_0^{(f)}\right) - l_1 - l_2\frac{4\mu\beta_0}{3h} = 0 \tag{4.23}$$

$$\frac{\partial \mathcal{L}}{\partial u_j^{(f)}} = -\hat{\rho}^{(f)} a_j^{(+)}\left(\tilde{u}_j^{(f)} - u_j^{(f)}\right) - l_2\frac{4\mu\beta_j}{3h} = 0 \quad j = 1,\ldots,r \tag{4.24}$$

$$\frac{\partial \mathcal{L}}{\partial \sigma_0} = \frac{a_0^{(-)}}{2\mu_e + \lambda_e}(\tilde{\sigma}_0 - \sigma_0) + l_2 = 0 \tag{4.25}$$

$$\frac{\partial \mathcal{L}}{\partial \rho_0^{(f)}} = a_0^{(-)}\frac{R\hat{T}^{(f)}}{M\hat{\rho}^{(f)}}\left(\tilde{\rho}_0^{(f)} - \rho_0^{(f)}\right) + l_2\frac{R\hat{T}^{(f)}}{M} = 0 \tag{4.26}$$

gives (4.13)–(4.15). Note that $a_0^{(-)} = a_0^{(+)}$, since the same summation by parts norm is used on the two domains. The interface conditions (4.18) and (4.19) are obtained from $\partial\mathcal{L}/\partial l_1 = 0$ and $\partial\mathcal{L}/\partial l_2 = 0$ respectively. Finally, insertion of (4.13)–(4.15) into these interface conditions gives (4.16) and (4.17). □

Note that by combining the velocities from (4.13) and (4.14), the common interface velocity can be written

$$\frac{\hat{\rho}^{(f)}\tilde{u}_0^{(f)} + m_0\tilde{u}_0^{(s)}}{\hat{\rho}^{(f)} + m_0} + l_2\frac{4\mu}{3}\frac{1}{\hat{\rho}^{(f)} + m_0}\frac{\beta_0}{a_0^{(+)}h}. \tag{4.27}$$

In the inviscid case, $\mu = 0$, (4.27) is the same mass weighted average for the boundary velocity that was independently derived from a characteristic boundary condition and proved to be stable for explicit time discretizations in [7]. Similarly, by using the notation

$$\tilde{\sigma}_0^{(f)} = -\frac{R\hat{\rho}^{(f)}}{M}T_0 - \frac{R\hat{T}^{(f)}}{M}\tilde{\rho}_0^{(f)} + \frac{4\mu}{3}D_R\tilde{u}_0^{(f)}$$

and

$$\hat{p}^{(f)} = \frac{R\hat{T}^{(f)}\hat{\rho}^{(f)}}{M}, \tag{4.28}$$

the common interface stress can be written

$$\frac{\hat{p}^{(f)}\tilde{\sigma}_0^{(s)} + (2\mu_e + \lambda_e)\tilde{\sigma}_0^{(f)}}{\hat{p}^{(f)} + 2\mu_e + \lambda_e} + (2\mu_e + \lambda_e)\frac{4\mu}{3}\left(\frac{l_1\beta_0}{a_0^{(+)}\hat{\rho}^{(f)}h} + l_2\frac{4\mu}{3\hat{\rho}^{(f)}h^2}\sum_{k=0}^{r}\frac{1}{a_k^{(+)}}\beta_k^2\right)$$

which again, in the inviscid case, is the same weighted average stress that was proved stable for explict time discretizations in [7].

4.2 Non-linear coupled problem

The straightforward generalization of (4.2) and (4.3) to the complete non-linear equations (3.1) and (3.2) is

$$\frac{d}{dt}\begin{pmatrix} u^{(s)} \\ \sigma \\ T^{(s)} \\ x \end{pmatrix}_j = \begin{pmatrix} \frac{1}{m_0}D_L\left(\sigma_j - p_j^{(s)}\right) \\ \frac{2\mu_e+\lambda_e}{D_L x_j}D_L u_j^{(s)} \\ \frac{\sigma_j - p_j^{(s)}}{m_0}D_L u_j^{(s)} + D_L\left(\frac{\kappa_e}{D_L x_j}D_L T_j^{(s)}\right) \\ u_j^{(s)} \end{pmatrix} \tag{4.29}$$

on $j \leq 0$, and

$$\frac{d}{dt}\begin{pmatrix}\rho^{(f)}\\ \rho^{(f)}u^{(f)}\\ e\end{pmatrix}_j + \begin{pmatrix} D_R\left(\rho_j^{(f)}u_j^{(f)} - u_0^{(f)}\rho_j^{(f)}\right)\\ D_R\left(\rho_j^{(f)}(u_j^{(f)})^2 + p_j^{(f)} - u_0^{(f)}\rho_j^{(f)}u_j^{(f)}\right) - \frac{4}{3}\mu D_R^2 u_j^{(f)}\\ D_R\left(u_j^{(f)}(e_j + p_j^{(f)}) - u_0^{(f)}e_j\right) - \frac{4}{3}\mu D_R\left(u_j^{(f)}D_R u_j^{(f)}\right) - D_R\left(\kappa D_R T_j^{(f)}\right)\end{pmatrix} = 0. \quad (4.30)$$

on $j \geq 0$. The grid derivative x_X was linearized to one in the analysis in Sec. 4.1, but it should be present in the full equations. Therefore, the temperature interface conditions also takes into account that the gradient is defined in the Eulerian frame, and become

$$T_0^{(s)} = T_0^{(f)} \qquad \kappa_e \frac{1}{D_L x_0} D_L T_0^{(s)} = \kappa D_R T_0^{(f)}, \quad (4.31)$$

which determine the two unknowns $T_0^{(s)}$ and $T_0^{(f)}$. The projection conditions (4.13)–(4.14) are kept without changes. There are several possibilities for the linearization density $\hat{\rho}^{(f)}$. In Section 5 we have used the value one point into the fluid, i.e., $\hat{\rho}^{(f)} = \rho_1^{(f)}$. Similarly, the linearization pressure needed below is set to $\hat{p}^{(f)} = p_1^{(f)}$ in the numerical experiments. (4.15) is replaced by the similar update for the pressure,

$$p_0^{(f)} = \tilde{p}_0^{(f)} - \hat{p}^{(f)} l_2 / a_0^{(+)}, \quad (4.32)$$

where

$$\tilde{p}_0^{(f)} = \frac{R\tilde{\rho}_0^{(f)} T_0}{M}.$$

The Lagrangian multipliers l_1 and l_2 are, in the non-linear case, computed as the solution of the system

$$\left(\frac{1}{m_0} + \frac{1}{\hat{\rho}^{(f)}}\right)\frac{l_1}{a_0^{(+)}} + \frac{4\mu}{3\hat{\rho}^{(f)}}\frac{\beta_0}{a_0^{(+)}h} l_2 = \tilde{u}_0^{(s)} - \tilde{u}_0^{(f)} \quad (4.33)$$

$$\frac{4\mu}{3\hat{\rho}^{(f)}}\frac{\beta_0}{a_0^{(+)}h} l_1 + \left(2\mu_e + \lambda_e + \hat{p}^{(f)} + \frac{16\mu^2}{9\hat{\rho}^{(f)}h^2}\sum_{k=0}^{r}\frac{a_0^{(+)}}{a_k^{(+)}}\beta_k^2\right)\frac{l_2}{a_0^{(+)}} = \tilde{\sigma}_0 + \tilde{p}_0^{(f)} - \frac{4\mu}{3} D_R \tilde{u}_0^{(f)}, \quad (4.34)$$

which is the same as (4.16) and (4.17), but with the second equation written in terms of the pressure. To summarize, the interface conditions for the non-linear coupled problem

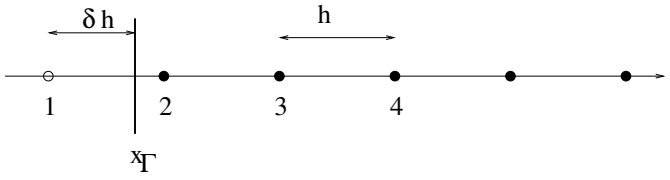

Figure 3: Grid points with boundary between points 1 and 2.

is (4.31), (4.13), (4.14), and (4.32), where the parameters l_1 and l_2 are determined by (4.33) and (4.34). Finally, after the fluid interface pressure and temperature are determined, the interface fluid density $\rho_0^{(f)}$, is adjusted to satisfy the perfect gas law.

Note that (4.32) is equivalent to the stress continuity condition

$$\sigma_0 = -p_0^{(f)} + \frac{4\mu}{3} D_R u_0^{(f)} \tag{4.35}$$

for any choice of linearization states $\hat{\rho}^{(f)}$ and $\hat{p}^{(f)}$. This is seen by using (4.14) and the stress update $\sigma_0 = \tilde{\sigma}_0 - (2\mu_e + \lambda_e) l_2 / a_0^{(+)}$ to eliminate $\tilde{u}_j^{(f)}$ and $\tilde{\sigma}_0$ from (4.34). In practical computations, we use (4.35) instead of (4.32) to determine $p_0^{(f)}$.

The interface is always located at $j=0$, but because the grid moves in both domains, a fixed boundary for the fluid in the Eulerian domain becomes a moving boundary in the frame of the grid, and has to be treated specially.

4.3 Wall boundary

In some of the numerical examples below, the grids are moving while the boundary of the computational domain is fixed. In this case the boundary condition at the fixed domain boundary is treated as a moving embedded boundary in the frame of the moving grid. The situation is outlined in Fig. 3. The points x_2, x_3, …, are interior to the computational domain, x_1 is the ghost point. The boundary is located at $x_\Gamma(t)$ and it is fixed, but when viewed in the moving grid frame, the location of the boundary obeys the equation

$$\frac{dx_\Gamma}{dt} = -s \tag{4.36}$$

where s is the velocity of the grid. Solving (4.36) together with the other equations determines the boundary location at each time level. In Fig. 3, the ghost point x_1 is the first point outside the domain. The distance between the ghost point and the boundary is denoted δh, where h is the grid spacing. The Dirichlet boundary condition

$$u(x_\Gamma) = g,$$

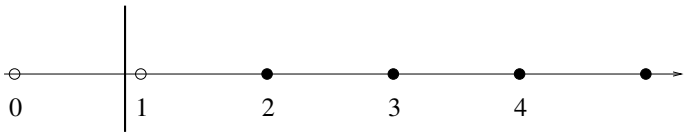

Figure 4: Boundary has moved backwards, 1 becomes interior point and 0 becomes the new ghost point.

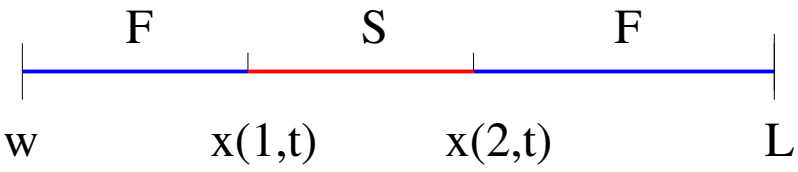

Figure 5: Computational domain for the numerical experiments.

with given data g, is imposed by the second order extrapolation formula

$$\frac{(1-\delta)(2-\delta)}{2}u_1+\delta(2-\delta)u_2+\frac{\delta(1-\delta)}{2}u_3+\eta(u_1-2u_2+u_3)=g. \tag{4.37}$$

η is an artificial parameter that is used to prevent division by zero, see [8]. The value of the solution at the ghost point, x_1, is found by solving (4.37) for u_1. A similar formula for Neumann boundary conditions is easily derived, see [9]. Equation (4.37) is straightforward to formally generalize to fourth order by increasing the extrapolation order, and the order of difference in the artificial term. This fourth order generalization worked well in the numerical experiments below, a proof of stability is outside the scope of this article.

If the boundary moves to the left in Fig. 3, it is possible that a ghost point becomes an interior point, and a new ghost point will have to be added. In Fig. 4, x_1 is the ghost point at time t_n that becomes an interior point at t_{n+1}, and x_0 becomes the new ghost point. To handle this, (4.37) is used to give values to both u_1 and u_0 at t_{n+1} (shifted one point left for u_0). δ will then be negative for x_1, but the coefficient in front of the ghost point, will be bounded away from zero, making it a well-defined boundary condition.

5 Numerical examples

The equations solved in this section are (4.29) and (4.30), coupled by the interface conditions described in Section 4.2. The time integration is explicit by the fourth-order accurate Runge-Kutta method. The time step is uniform in the domain, and determined as the smallest of the time steps required by the CFL constraints from the convection in the fluid, the diffusion in the fluid, the elastic wave speed in the solid, and the heat diffusion in the solid. The CFL number is 0.8. The computational domain is $w<x<L$, in the Eulerian coordinate. The domain of the fluid equations is $X<1$ and $2<X$, the domain for

the solid equations is $1<X<2$. The grid mapping for the fluid is $x=X-1+x(1,t)$ and $x=X-2+x(2,t)$ for the left and right part of the fluid respectively. The lower and upper boundaries $x=w$ and $x=L$ are embedded boundaries, as described in Section 4.3. The grid sizes in the computations below are always such that the two fluid/solid interfaces at $X=1$ and $X=2$ coincide with grid points. Figure 5 outlines the computational domain.

5.1 Test with the method of manufactured solutions

The implementation and formal accuracy is first verified by the method of manufactured solutions. Forcing functions on the right hand side of the equations are determined to give the exact solutions

$$\rho^{(f)}=1+\frac{1}{2}\sin(\omega X)\cos(t) \tag{5.1}$$

$$u^{(f)}=\sin(t)\cos(\omega X+\phi) \tag{5.2}$$

$$T^{(f)}=10+\sin(3t)\cos(2X) \tag{5.3}$$

in the fluid, and

$$u^{(s)}=dx(X,t)/dt \tag{5.4}$$

$$\sigma=\sin(t^2)\sin(\omega X) \tag{5.5}$$

$$T^{(s)}=5+\cos(t)\sin(3X) \tag{5.6}$$

$$x(X,t)=X+\frac{t^2}{2}(1+X+\epsilon\sin(2\pi X)) \tag{5.7}$$

in the solid. The computational domain is $1/4<x<4$ with the solid in $1<X<2$. The exact solution is enforced by Dirichlet boundary conditions at the embedded boundaries at $x=1/4$ and $x=4$. The interface conditions are enforced at $X=1$ and $X=2$. The parameter values $\epsilon=0.2$, $\omega=2$, $\phi=0.47$ are used. The material parameters are set to, $2\mu_e+\lambda_e=10$, $\mu=0.01$, $\kappa=0.03$, $\kappa_e=0.02$, $\alpha=1$, $R/M=1$, $m_0=2$, $\gamma=1.4$. At the fluid/solid interfaces, the manufactured solutions are not continuous. The jump is prescribed as a forcing in the interface conditions, e.g., $u_0^{(f)}-u_0^{(s)}=g_u(t)$, where g_u is the jump in the velocity at the interface. These forcings are straightforward to introduce into the interface conditions. Figure 6 shows the errors in L^2-norm in the fluid and solid parts of the domain at time 0.45 for a sequence of computations with increasing grid refinements. The coarsest grid has $h=0.05$, which corresponds to 75 grid points in the domain. The formal orders of the summation by parts difference operators are given as two numbers, x/y, for interior accuracy x and boundary accuracy y. The higher order methods $6/3$ and $8/4$ are clearly seen to give more accurate results than $2/1$ and $4/2$. The formal order in the boundary conditions at the embedded boundaries $x=w$ and $x=L$ are two for the $2/1$ and $4/2$ methods, and four for the $6/3$ and $8/4$. The explanation for the small difference in results

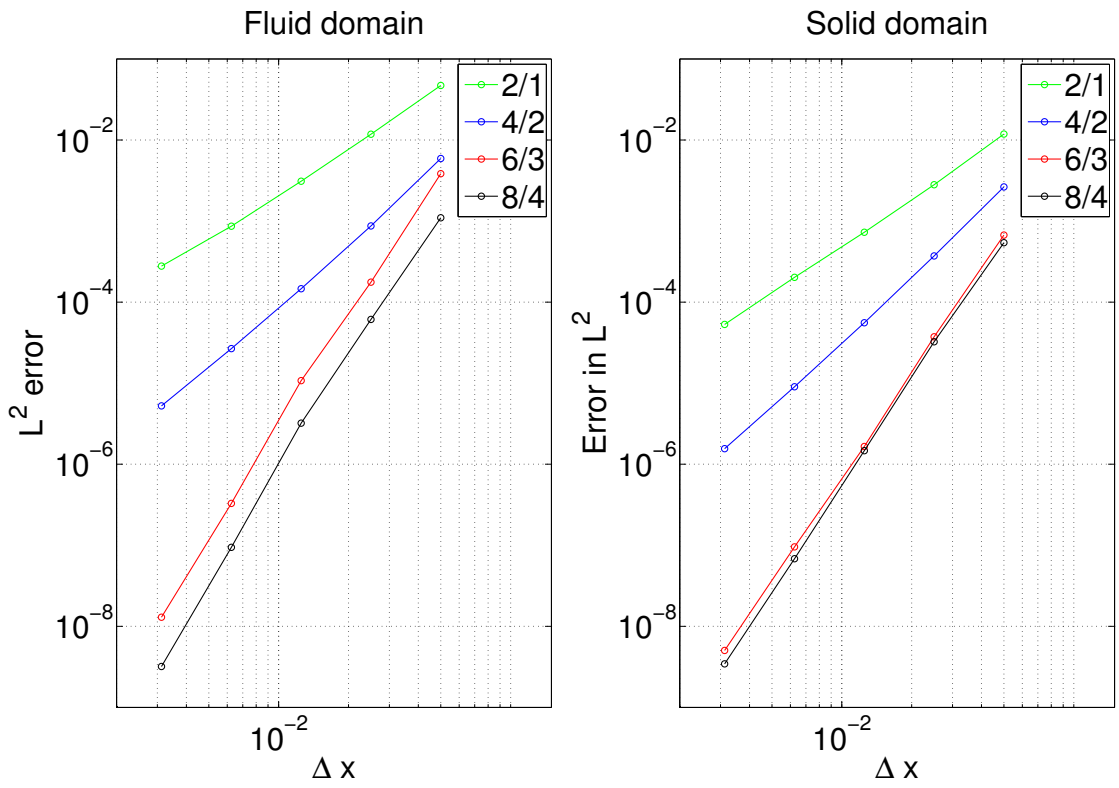

Figure 6: Errors in solution at time 0.45 in L^2-norm for the fluid domain (left) and solid domain (right). Summation by parts finite difference approximation of formal orders interior/boundary, 2/1 (green), 4/2 (blue), 6/3 (red), and 8/4 (black).

with 6/3 and 8/4 could be that the errors from the embedded boundaries dominate over other errors on fine grids.

In hyperbolic problems with exact Dirichlet inflow data, there is a gain of one order in the numerical boundary conditions, so that the 8/4 method should converge with 5th order, the 6/3 with 4th order, etc. However at the fluid/solid interface the situation is not necessarily the same, because the imposed data at inflow is the value of the outflow variable of the neighboring domain. Therefore any error in the outflow variable from one domain, is transmitted to the inflow boundary on the other domain. Furthermore, in the computations here there are also diffusion terms present in the equations. Assuming local errors of order p at the boundary and/or interfaces for the $2p/p$ method, the L^2 norm error would have convergence exponent of $p+1/2$. The observed convergence rates presented in Table 1 are in reasonable agreement with this, only the 6/3 method converges somewhat faster than expected. There is reasonable confidence that the implementation is correct.

	Fluid				Solid			
Order	8/4	6/3	4/2	2/1	8/4	6/3	4/2	2/1
Conv. exp.	4.9	4.7	2.4	1.6	4.3	4.1	2.6	1.8

Table 1: Observed convergence exponents in L^2-norm between the two finest grids.

Fig. 7 shows the error vs. the CPU time for five different grid sizes. The error is computed as the maximum of the L^2 errors over the two domains. Figure 7 clearly shows that the higher order schemes are more efficient than the lower order schemes. The gain in CPU time with the higher order schemes becomes larger as the desired error level is made smaller.

5.2 Elastic rod in compressible fluid

Consider a test with an elastic rod in a compressible fluid. There is a gravitational force acting in the negative x-direction. The domain is the same as outlined in Fig. 5, with a solid wall boundary at $w=0$, where adiabatic boundary conditions are imposed. The upper boundary of the fluid, $L=6$, is treated as an open boundary with the artificial boundary conditions described in [5]. Initially the rod at rest is released and falls by its own weight towards the lower boundary $x=0$. The fluid to the left of the rod is heated and compressed as it moves left. Eventually the rod bounces back right and a new cycle of left/right movement begins. Figures 8a–8d display the temperature during the left/right cycle. Red indicates the elasticity equations and blue the Navier-Stokes equations. The material parameters for the elastic material are

$$\kappa_e=0.5,\ 2\mu_e+\lambda_e=10^5,\ m_0=2700,\ \alpha=1$$

and the pressure is identically zero, i.e., the material is purely elastic. The gravitational force is set as $f^{(s)}=-10$ (see (2.1)). The material parameters for the fluid are

$$\mu=0.5\ ,\kappa=0.7,\ \gamma=1.4,\ R/M=8.3145/0.029$$

These values were selected to obtain visible effects of many aspects of the equations, over a reasonable time. They do not necessarily represent physically reasonable materials. Figure 8a shows how the gas to the left is heated and compressed during the left movement. The leftmost point is reached in Fig. 8b. During the right movement in Fig. 8c, the gas is cooled by expansion. Back at the original position, shown in Fig. 8d, a minor temperature peak remains because the solid is not cooled as quickly as the fluid. Figure 9 shows the velocity for the same computation at the same times as the temperatures in Fig. 8. The movement of the object is illustrated by inspecting the magnitude and direction of the velocity. Fig. 10 gives another illustration of the bouncing character of the solution, by displaying the positions of the two interfaces as function of time. The

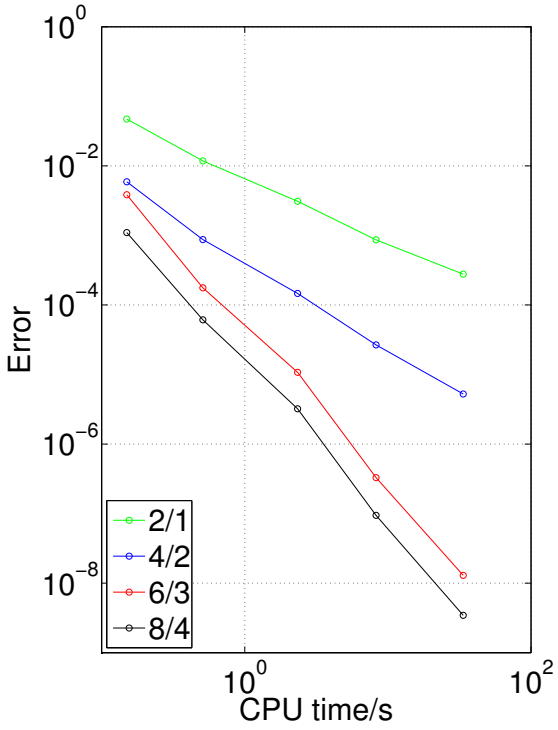

Figure 7: L^2-norm errors vs. CPU time. Summation by parts finite difference approximation of formal orders interior/boundary, 2/1 (green), 4/2 (blue), 6/3 (red), and 8/4 (black).

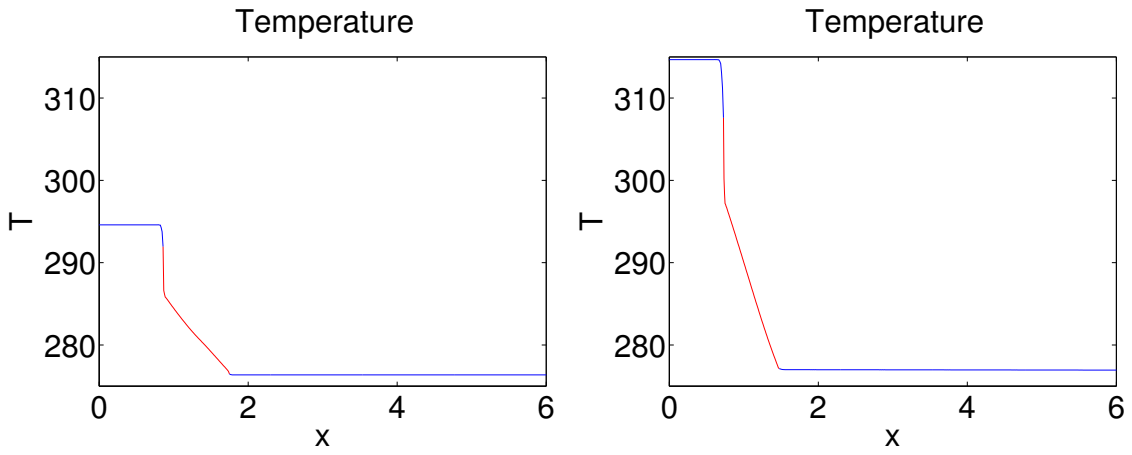

(a) t=0.230 moving left.

(b) t=0.461 leftmost position.

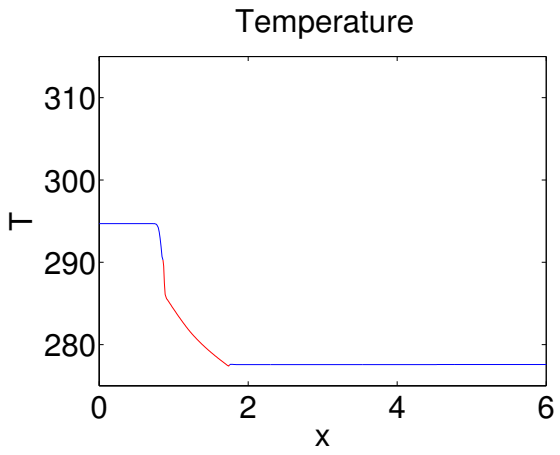

(c) t=0.681 moving right.

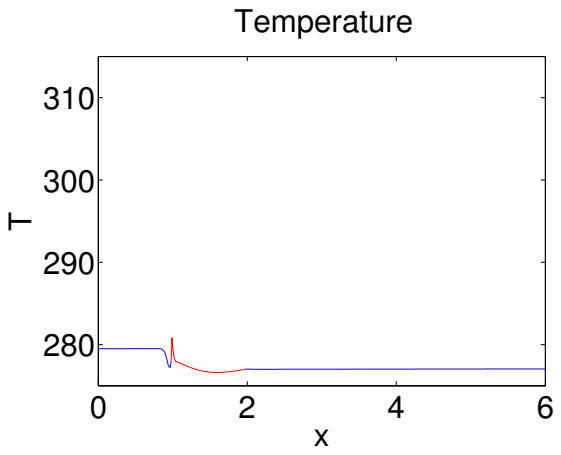

(d) t=0.908 rightmost position.

Figure 8: Temperature of the falling rod problem at four different times using the $4/2$ method and $h = 0.0125$. Blue and red represent fluid and solid quantities respectively.

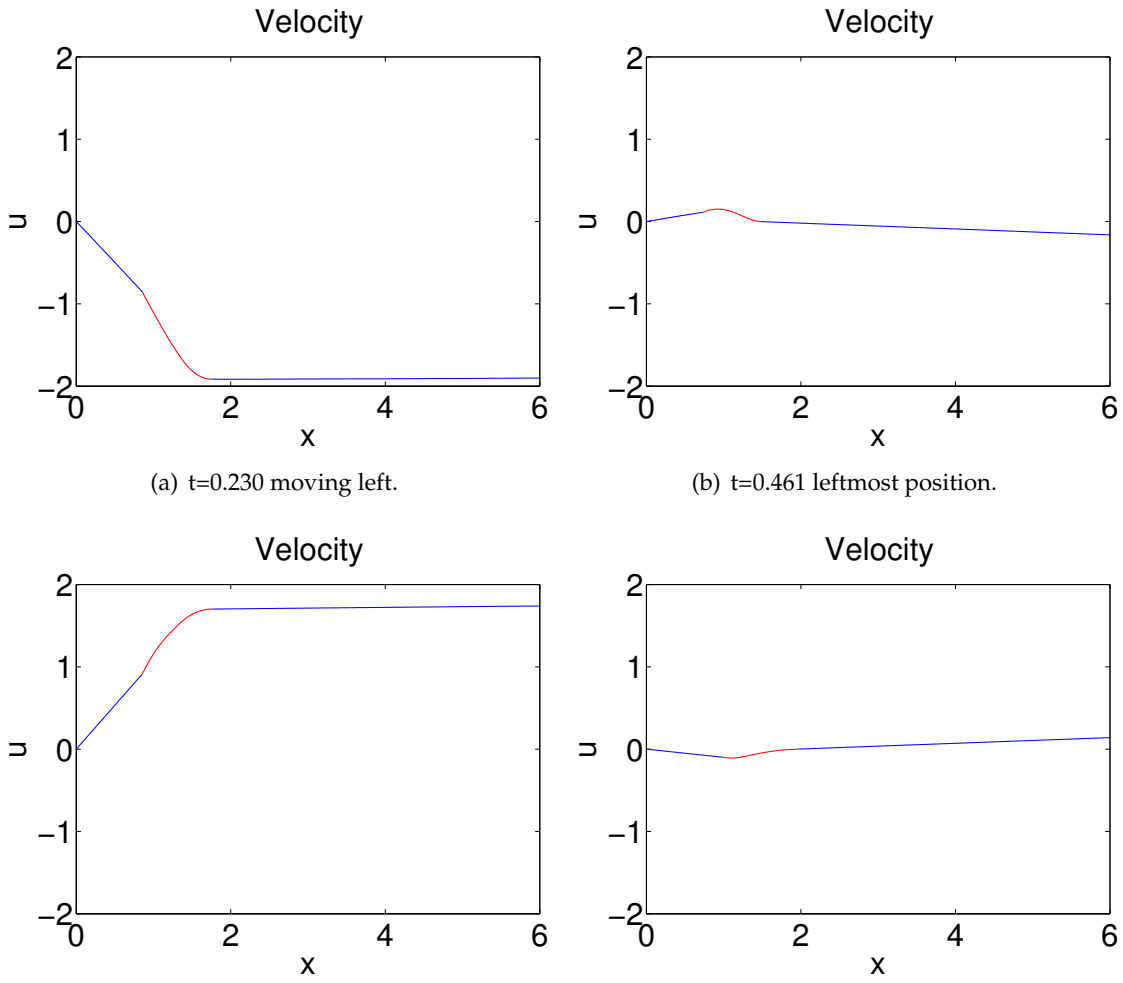

(a) t=0.230 moving left.

(b) t=0.461 leftmost position.

(c) t=0.681 moving right.

(d) t=0.908 rightmost position.

Figure 9: Velocity of the falling rod problem at four different times using the $4/2$ method and $h=0.0125$. Blue and red represent fluid and solid quantities respectively.

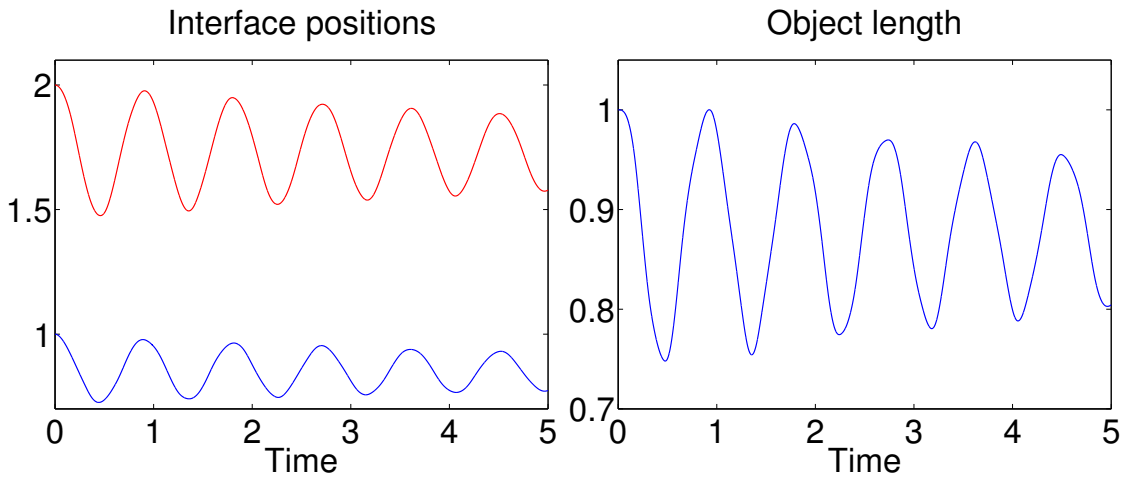

Figure 10: The position of the two fluid/solid interfaces as function of time (left), and the length of the rod as function of time (right). The 4/2 method with $h=0.0125$ was used.

figure shows how the dissipation mechanisms acts to reduce the oscillation amplitude with time. The right subfigure shows the length of the object, computed as the difference between the two positions in the left subfigure. The computations in Figs. 8–10 were all made using the 4/2 method on a grid with $h=0.0125$.

Finally in Fig. 11 we show a closeup of the velocity near the lower fluid/solid interface at time 0.908 computed using grids of different resolutions. Results are presented for each of the three methods of formal accuracy 2, 4, and 6 (away from the boundaries). The reference solution, shown in black, was obtained with an extreme resolution, and verified to not change visibly in the plot under a factor two of grid refinement. The results with a coarser resolution of $h=0.05$, shown in cyan/magenta (for fluid/solid), are compared with results obtained with the finer resolution $h=0.025$, shown in blue/red (for fluid/solid). From Fig. 11 we infer that the higher order methods show considerably faster grid convergence than the second order method. The 6/3 method shows somewhat better convergence than the 4/2 method, but as shown in Fig. 6, the difference would be more pronounced if the grids were refined further.

6 Conclusions

We have presented stable interface conditions for fluid/structure coupling in the context of high order accurate finite difference schemes. The method has been developed in a Lagrangian formulation for the equations of elasticity. The fluid solution is computed using the Navier-Stokes equations on a moving grid. The interface conditions, which includes viscous effects and heat conduction, is proved to be linearly stable for semi-

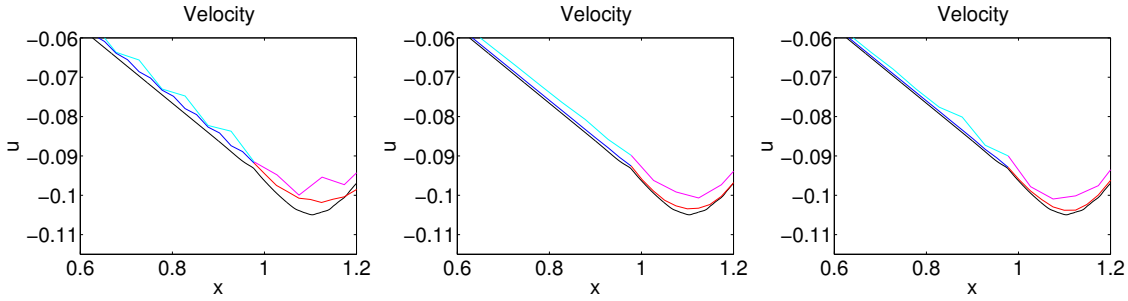

(a) 2/1 method (b) 4/2 method (c) 6/3 method

Figure 11: Grid convergence study. Close up view of the velocity at time 0.908 for $h = 0.05$ (fluid-cyan, solid-magenta), $h = 0.025$ (fluid-blue, solid-red). Reference solution shown in black.

discrete approximations through norm estimates. Numerical experiments have shown the method to be stable with explicit time stepping up to the CFL limit given by the methods in the two subdomains. The interface conditions do not require any additional time step reduction.

We are currently generalizing the interface conditions to two and three space dimensions. If symmetrizers can be found for the multidimensional equations, the norm estimate technique presented here generalizes straightforwardly. The linearized three dimensional Navier-Stokes equations have known symmetrizers, see [1]. Symmetrizers for the three dimensional equations of linear elasticity are also well known. However, we have found that the linearization of the system (2.1) cannot be symmetrized as a result of the the term $W\sigma + \sigma W^T$ associated with the Jaumann objective rate. We are therefore investigating properties of alternative models for the objective rate. The results of these multi dimensional investigations will be reported in a forthcoming paper.

In this work we have only considered smoothly varying flow variables. However, there are many applications of fluid structure interaction where high-speed flows and shock waves are of interest. Such flows can be computed by hybridizing the stable and accurate methods developed here with a more robust but less accurate shock capturing scheme. This is a well-known technique for computing compressible flows with both shock waves and small scale oscillatory behavior, see, e.g., [14].

Acknowledgements

This study has been supported by Lawrence Livermore National Laboratory under the auspices of the U.S. Department of Energy through contract number DE-AC52-07NA27344.

References

[1] S. Abarbanel and D. Gottlieb. Optimal time splitting for two- and three-dimensional Navier-Stokes equations with mixed derivatives. *J. Comput. Phys.*, 41:1–33, 1981.

[2] T. Belytschko, W. K. Liu, and B. Moran. *Nonlinear Finite Elements for Continua and Structures*. John Wiley & Sons Ltd., 2000.

[3] M. H. Carpenter, D. Gottlieb, and S. Abarbanel. Time-stable boundary conditions for finite-difference schemes solving hyperbolic systems: Methodology and application to high-order compact schemes. *J. Comput. Phys.*, 111:220–236, 1994.

[4] G. S. Chesshire and W. D. Henshaw. Composite overlapping meshes for the solution of partial differential equations. *J. Comput. Phys.*, 90(1):1–64, 1990.

[5] L. Halpern. Artificial boundary conditions for incompletely parabolic perturbations of hyperbolic systems. *SIAM J. Math. Anal.*, 22:1256–1283, 1991.

[6] W. D. Henshaw and K. K. Chand. A composite grid solver for conjugate heat transfer in fluid-structure systems. *J. Comput. Phys.*, 228:3708–3741, 2009.

[7] J.W.Banks and B.Sjögreen. Stability of numerical interface conditions for fluid/structure interaction. *Commun. Comput. Phys.*, 10:279–304, 2011.

[8] H.-O. Kreiss and N. A. Petersson. A second order accurate embedded boundary method for the wave equation with Dirichlet data. *SIAM J. Sci. Comput.*, 27:1141–1167, 2006.

[9] H.-O. Kreiss, N. A. Petersson, and J. Yström. Difference approximations of the Neumann problem for the second order wave equation. *SIAM J. Numer. Anal.*, 42:1292–1323, 2004.

[10] S. Nilsson, N. A. Petersson, B. Sjögreen, and H.-O. Kreiss. Stable finite difference approximations for the elastic wave equation in second order formulation. *SIAM J. Numer. Anal.*, 45:1902–1936, 2007.

[11] P. Olsson. Summation by parts, projections, and stability. I. *Math. Comput.*, 64:1035–1065, 1995.

[12] B. Sjögreen and N.A.Petersson. A fourth order accurate finite difference scheme for the elastic wave equation in second order formulation. *J. Sci. Comp.*, 2011. LLNL-JRNL-483427.

[13] B. Sjögreen and H. C. Yee. On skew-symmetric splitting and entropy conservaton schemes for the euler equations. In *Proceedings of ENUMATH09*, Uppsala, Sweden, June 29 - July 3 2009.

[14] B. Sjögreen and H.C. Yee. Multiresolution wavelet based adaptive numerical dissipation control for shock-turbulence computation. *J. Sci. Comp.*, 20:211–255, 2004.

[15] B. Strand. Summation by parts for finite difference approximations for d/dx. *J. Comput. Phys.*, 110:47–67, 1994.

[16] M. L. Wilkins. *Computer simulation of dynamic phenomena*. Springer, 1999.